Nanoscale Advances

ROYAL SOCIETY OF CHEMISTRY

PAPER

View Article Online
View Journal | View Issue

Cite this: *Nanoscale Adv.*, 2026, **8**, 1585

L-Arg@ZY-Fe_3O_4 mesoporous nanomaterial: a novel magnetically recoverable bio-organocatalyst for three-component synthesis of 4*H*-pyran and -chromene derivatives

Mehdi Kalhor * and Samira Zebardast

Received 28th November 2025
Accepted 21st January 2026

DOI: 10.1039/d5na01102g

rsc.li/nanoscale-advances

In this project, a novel hybrid nanostructure L-arginine-modified magnetic zeolite-NaY (Arg@zeolite-Y-Fe_3O_4) was successfully designed and synthesized. It was further characterized using standard analytical techniques including FT-IR, FE-SEM, EDX, BET, TEM, XRD, VSM and TGA. The resulting magnetic mesoporous material was employed as a highly active organocatalyst for the synthesis of chromene analogues *via* a one-pot, three-component reaction between aldehydes, malononitrile and either phenols or active methylene reagents (*e.g.*, dimedone) under aqueous conditions. This nanocatalyst offers several notable advantages: facile and cost-effective synthesis, environmentally friendly reaction conditions, excellent catalytic performance, and easy magnetic separation. Moreover, it demonstrates remarkable recyclability with minimal loss of activity over multiple cycles. The use of water as a green solvent, along with high product yields and benign operational conditions, highlights the sustainable and practical nature of this catalytic system.

1. Introduction

In recent years, heterogeneous nanocatalysts have brought about a significant transformation in the synthesis of organic compounds due to their unique properties. These include enhanced reaction rates and selectivity, high surface-to-volume ratios, facile separation from the reaction medium, and excellent recyclability.[1–5] Such advantages have made the design and development of environmentally friendly heterogeneous nanocatalysts a central focus in green chemistry research.[6,7] A promising approach in this field is the development of multifunctional nanocatalysts that incorporate diverse active sites within a single structure. These systems are particularly effective in multistep reactions requiring either similar or distinct catalytic sites in a single reaction vessel.[8–11] Among various solid supports, zeolites have emerged as ideal platforms for anchoring organic catalysts. Zeolite-NaY and its modified derivatives with organic and inorganic functional groups have attracted considerable attention due to their high surface area, tunable pore size in the mesoporous range, strong hydrothermal stability, adjustable acidity, and low cost. These advantageous properties render zeolites invaluable across various industrial and research applications.[12–17] Despite the numerous advantages of heterogeneous catalysts, one of the major challenges in their application at both laboratory scale and in industrial processes is the difficulty of separating them from the reaction medium for recovery and reuse. An effective strategy to address this limitation involves imparting magnetic properties to heterogeneous nanocatalysts. Recent studies have shown that immobilizing magnetic nanoparticles onto a solid support *via* a core@mesoporous approach not only enables their efficient performance as Lewis acid catalysts in organic reactions, but also facilitates the rapid and straightforward separation of the catalyst from the reaction mixture using an external magnetic field. On the other hand, magnetic nanostructures (MNPs) have attracted remarkable attention in recent years owing to their wide-ranging potential in biomedical applications. These applications span targeted drug delivery, magnetic resonance imaging (MRI), biomolecular sensing, and biological as well as magnetic separation processes, among others.[18–24] In addition, the application of magnetic nanocatalysts has emerged as a rapidly growing field aimed at developing sustainable and environmentally benign synthetic methodologies.

Recently, the use of amino acids as green bio-organic catalysts has recently drawn extensive attention in the field of organic chemistry. Amino acids are interested in catalytic reactions by researchers due to their unique properties including non-toxicity, safety, bi-functional catalyst due to the existence of both Lewis basic (NH_2) and Brønsted acidic (COOH) sites and compatibility with many other materials.[25–31] However, separation of amino acids from the reaction mixture and their

Department of Chemistry, Payame Noor University, Tehran, 19395-4697, Iran. E-mail: mekalhor@pnu.ac.ir; mekalhor@gmail.com; Fax: +98 2537179170; Tel: +98 2537179170

no-reusability after one reaction are major problems for their catalytic applications. A good idea to overcome these limitations is the immobilization of homogeneous organocatalysts to high-surface-area solid supports such as polymers, nanosilica, zeolites and metal oxides.[32–34] Arginine plays a pivotal role in catalyst design, particularly in enhancing catalytic efficiency and structural stability. Its multifunctional nature allows it to be anchored onto heterogeneous solid supports such as graphitic carbon nitride or magnetic nanoparticles to modify surface properties, thereby improving the reactivity and selectivity of catalysts in the synthesis of heterocyclic compounds. Moreover, arginine has found applications in electrocatalysis, serving as both a reducing agent and a structural directing component, as well as in enzyme catalysis, where it contributes to biomimetic activity and functional performance.[35–39] To the best of the authors' knowledge, the use of arginine-functionalized magnetic nanozeolite-NaY as efficient multifunctional nanocatalyst for the synthesis of 4*H*-chromene derivatives has not yet been reported. In contrast to previously reported L-arginine-based catalytic systems, the present L-Arg@ZY-Fe_3O_4 nanomaterial integrates bio-organocatalytic functionality, magnetic recoverability, and Lewis acidic sites within a single heterogeneous platform. The ultrasonic-assisted immobilization of Fe_3O_4 nanoparticles ensures their stable incorporation into the zeolite Y framework, leading to enhanced catalytic performance, facile separation, and improved reusability.

Between the oxygen-containing heterocycles, fused benzo-4*H*-pyran, namely, 4*H*-chromene moieties are imperative organic compounds due to their biological activity and pharmaceutical applications. They are also used in the field of cosmetic agents, laser dyes, pigments and potential biodegradable agrochemicals.[40–43] Fig. 1 depicts a representative set of naturally occurring compounds that are broadly distributed across plants, animals, and diverse microorganisms. In addition, it highlights candidate molecular frameworks for commercial drugs with a wide spectrum of biological activities, all of which are unified by the presence of the pyran or chromene core. Accordingly, the synthesis of these organic frameworks using new green and environmentally friendly routes is valuable and necessary.

One of the general methods for synthesis of 2-amino-chromenes is the condensation of aldehyde derivatives, malononitrile and diverse electron-rich phenolic C–H activated or enolizable acidic compounds in presence of homogeneous and heterogeneous catalysts.[44–63] Although some of these catalytic methods have advantages, there are still some problems in the synthetic process such as the use of hazardous organic solvents, consumption of energy inputs for heating of the reaction system, the use of transition metal catalysts with the possibility of metal leaching in the reaction medium, the use of fuming or expensive catalysts with low reusability, and long reaction times. Therefore, the design of an effective, the facile and clean protocols for the preparation of 4*H*-chromenes is still needed especially by using greener reaction pathways and safer organocatalysts.

Considering the significance of 4*H*-chromenes, the efficiency of heterogeneous magnetic nanocatalysts in chemical processes, and in continuation of previous studies in this field,[9,64,65] we herein introduce a novel, efficient, and green catalytic methodology for the synthesis of 2-amino-4-aryl-3-cyanochromenes. This approach employs a robust and heterogeneous zeolite-NaY nanocatalyst magnetically modified with the amino acid arginine, operating in an aqueous medium at ambient temperature. The newly developed bio-organocatalyst exhibits excellent catalytic performance in the three-component cyclocondensation of aromatic aldehydes, malononitrile, and activated phenols or dimedone, enabling the synthesis of a wide range of 2-aminochromenes in very high yields (Scheme 1).

2. Experimental

2.1. Chemicals and apparatus

All chemicals were purchased from the Merck and Fluka Chemical Companies. Progress of the catalytic process was monitored by thin layer chromatography (TLC) using silica gel plates in the solvent system (ethyl acetate/*n*-hexane, 2 : 1). FT-IR spectra of the samples were obtained with KBr disc on a JASCO: FT-IR 4200-A spectrophotometer. ^{1}H NMR and ^{13}C NMR spectra were recorded on Bruker spectrophotometer (300 and 400 MHz) in DMSO-d_6 using Me_4Si as internal standard. Field emission-scanning electron microscopic (FE-SEM) images were performed on a Zeiss Sigma FE-SEM that it equipped with energy dispersive X-ray spectrometer (EDX). BET surface area and porosity analysis was carried out at 196 °C by a Japan Belsorp II

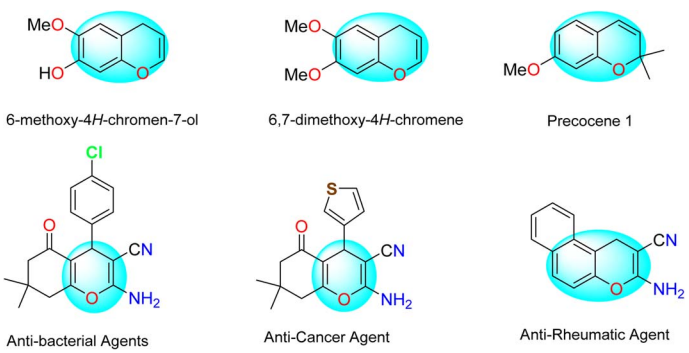

Fig. 1 Some naturally occurring and biologically-active structures with the chromene basic skeleton.

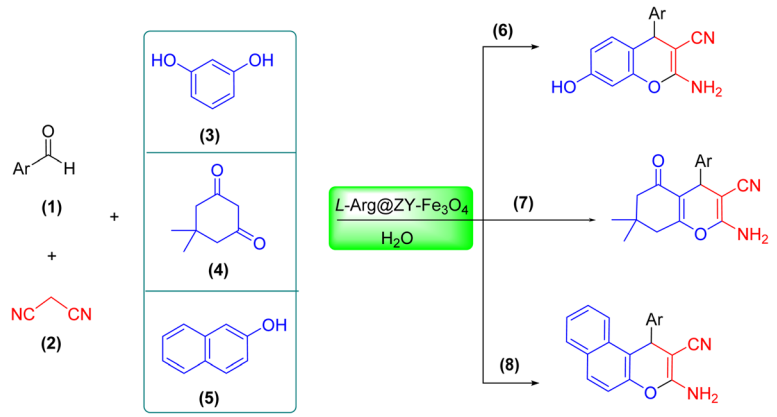

Scheme 1 Synthesis of 2-amino-chromenes catalyzed by Arg@ZY-Fe_3O_4 in aqueous medium.

system after the samples were vacuum dried at 150 °C overnight. The TGA/DTA measurements were carried out by using a Bahr (Wetzlar, Germany) STA-503 instrument. TGA/DTA runs were recorded at a scan rate of 10° min^{-1} up to 700 °C under pure argon atmosphere. Zeolite-Y-based nanocomposites were characterized using a Holland Philips X'Pert X-ray powder diffractometer equipped with CuKα radiation (λ = 0.154056 nm). The diffraction patterns were recorded over a 2θ range of 10° to 100° at a scanning rate of 2° min^{-1}. Magnetic properties of the samples were evaluated at room temperature using a vibrating sample magnetometer (VSM, 4-inch model, NDKF, Kashan University, Iran).

2.2. Synthesis of L-Arg@zeolite-NaY

The chloropropyl grafted zeolite-NaY (pCl@zeolite-NaY) was prepared according to a method described elsewhere.[64] Then, for the synthesis of pCl@zeolite-NaY attached with amino acid, in 100 mL round-bottom flask, 1 g pCl@zeolite-NaY was dispersed in 30 mL of toluene and stirred for 10 min under N_2 atmosphere. Next, 1.5 g (8.6 mmol) of arginine was added to solution in the presence of NEt_3 (1.2 mmol) and stirred under reflux conditions for 48 h. The resulting mixture was centrifuged, washed several times with toluene and distilled water under ultrasound irradiations and dried in oven at 70 °C for 2 h to produce the Arg@zeolite-NaY.

2.3. Synthesis of the final magnetic nanocatalyst: L-Arg@zeolite-Y-Fe_3O_4

To prepare the final magnetic nanocatalyst, 1.0 g of the previously synthesized nanocomposite (Arg@zeolite-NaY) was dispersed in 50 mL of distilled water using an ultrasonic bath to ensure uniform suspension. Subsequently, 1.0 mmol of $FeCl_2 \cdot 4H_2O$ and 2.0 mmol of $FeCl_3 \cdot 6H_2O$ were added to the dispersion and stirred at 60 °C. Under a nitrogen atmosphere, a 25% aqueous ammonia solution was introduced dropwise while maintaining continuous stirring. After approximately 30 minutes, the onset of the reaction led to the formation of Fe_3O_4 nanoparticles, indicated by a distinct color change from brown to dark black. Simultaneously, the nanoparticles were incorporated into the zeolite cavities. The resulting black precipitate was magnetically separated from the reaction mixture, thoroughly washed with distilled water to remove residual ions and impurities, and dried in an oven at 60 °C for 5 hours to obtain the final product (Scheme 2).

2.4. General procedure for the catalytic synthesis of 2-amino-chromenes

A mixture of aromatic aldehyde (1 mmol), malononitrile (1 mmol), phenols (resorcinol or 2-naphthol) or dimedone (1 mmol), and nano Arg@ZY-Fe_3O_4 (14 mg, 10% wt/wt) was stirred in aqueous medium at 90 °C for desired time (Table 1). After the satisfactory completion of the reaction, as indicated by TLC monitoring (*n*-hexane and ethyl acetate (2 : 1) as eluents), the reaction mixture was filtered and then the resulting solid was solved in EtOH. The nanocatalyst was separated from the solution using an external magnet. The filtrate was added to 10 mL of cold water and precipitate was filtered off and washed with cold ethanol–water mixture. The final product was obtained in most cases in pure form. However, if necessary, recrystallization could be performed in ethanol–water mixtures. All pure products are known and were identified by comparison of their melting point, FT-IR and ^{1}H NMR with those of authentic samples.

2.5. Spectroscopic data for selected compounds

2.5.1. 2-Amino-4-(2,4-dichlorophenyl)-7-hydroxy-4*H*-chromene-3-carbonitrile (6c). FT-IR (KBr, ν_{max}): 3477 (NH_2), 3044, 2937 (C–H), 2227 (CN), 1580, 1453, 1380 (C=C), 1290, 1217, 1144 (C–O), 1109, 1050 (C–N), 866, 821 (C–Cl), 620 cm^{-1}; ^{1}H NMR (400 MHz, DMSO-d_6): δ_H 9.77 (br, 1H, OH), 7.57–7.37 (m 2H, H-Ar), 7.21 (d, J = 8.40 Hz, 1H, H-Ar), 6.98 (s, 2H, NH_2), 6.71 (d, J = 8.40 Hz, 1H, H-Ar), 6.48–6.39 (m, 2H, H-Ar), 5.11 (s, 1H, CH) ppm.

2.5.2. 2-Amino-7-hydroxy-4-(4-methoxyphenyl)-4*H*-chromene-3-carbonitrile (6h). FT-IR (KBr, ν_{max}): 3391 (NH_2), 3046, 2921 (C–H), 2352 (CN), 1601, 1513, 1468, 1407 (C=C), 1278, 1172 (C–O), 1010 (C–N), 844, 813, 741, 480 cm^{-1}; ^{1}H NMR (400 MHz, DMSO-d_6): δ_H 9.67 (s, 1H, OH), 7.09 (d, J = 7.20 Hz,

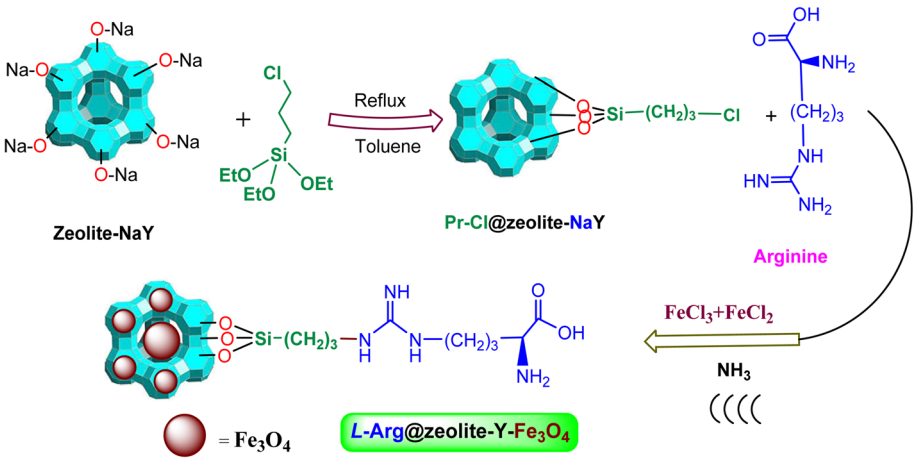

Scheme 2 The procedure for the preparation of Arg@zeolite-NaY.

Table 1 Porosimetry data from BET analysis for zeolite-NaY and Arg@ZY-Fe_3O_4

Samples	S_{BET}[a] ($m^2\ g^{-1}$)	V_{BJH}[b] ($cm^3\ g^{-1}$)	D_{Aap}[c] (nm)	W_{BJH}[d] (nm)	V_p[e] ($cm^3\ g^{-1}$)
Zeolite-NaY	441.3	0.032	2.213	6.73	0.2434
Arg@ZY-Fe_3O_4	127.4	0.009	6.703	2.41	0.2630

[a] Specific surface area. [b] Pore volume. [c] Adsorption average pore diameter ($4V/A$ by BET). [d] BJH adsorption average pore width ($4V/A$). [e] Total pore volume ($p/p_0 = 0.990$).

3H, H-Ar), 7.04 (s, 1H, H-Ar), 6.82 (s, 2H, NH_2), 6.77 (d, J = 8.40 Hz, 1H, H-Ar), 6.47 (d, J = 8.00 Hz, 1H, H-Ar), 6.39 (s, 1H, H-Ar), 4.55 (s, 1H, CH), 2.22 (s, 3H, OCH_3) ppm.

2.5.3. 2-Amino-7,7-dimethyl-5-oxo-4-phenyl-5,6,7,8-tetrahydro-4*H*-chromene-3-carbonitrile (7a). FT-IR (KBr, ν_{max}): 3395, 3323, 3212 (NH_2), 2960 (C–H), 2199 (CN), 1681 (C=O), 1660, 1597, 1371 (C=C), 1248, 1213 (C–O), 1036 (C–N), 695 cm^{-1}; ^1H NMR (500 MHz, DMSO-d_6): δ_H 7.28 (t, J = 7.20 Hz, 2H, H-Ph), 7.21–7.15 (m, 3H, H-Ph), 6.98 (s, 2H, NH_2), 4.20 (s, 1H, CH), 2.53 (s, 2H, CH_2), 2.27 (d, J = 16.05 Hz, 1H, CH_2), 2.12 (d, J = 16.05 Hz, 1H, CH_2), 1.06 (s, 3H, CH_3), 0.97 (s, 3H, CH_3) ppm; ^{13}C NMR (125 MHz, DMSO-d_6): δ_C 195.6 (C=O), 158.5, 162.5, 144.7, 128.3, 127.1, 126.6, 119.7, 112.8, 58.4, 50.0, 35.6, 31.8, 28.4, 26.8 ppm.

2.5.4. 3-Amino-1-(2-chlorophenyl)-1*H*-benzo[*f*]chromene-2-carbonitrile (8b). ^1H NMR (DMSO-d_6, 500 MHz): δ_H 7.96–7.90 (m, 2H, H-Ar), 7.64 (d, J = 8.45 Hz, 1H, H-Ar), 7.46–7.40 (m, 3H, H-Ar), 7.34 (d, J = 8.85 Hz, 1H, H-Ar), 7.18 (t, J = 3.90 Hz, 1H, H-Ar), 7.04 (d br, 3H, H-Ar and NH_2), 5.71 (s, 1H, CH) ppm; ^{13}C NMR (125 MHz, DMSO-d_6): δ_C 159.9, 151.5, 147.2, 142.6, 131.1, 130.8, 130.1, 128.7, 128.5, 128.2, 119.9, 118.4, 116.8, 114.8, 114.0, 112.5, 59.2, 35.1 ppm.

3. Results and discussion

3.1. Catalyst characterization

The Arg@ZY-Fe_3O_4 nanocomposite was prepared as depicted in the Scheme 2. First, the PrCl@zeolite-Y nanocomposite was produced by modifying zeolite-Y with the ($(EtO)_3$Si-PrCl) linker. The subsequent reaction between the amino acid arginine and Pr-Cl@Z-Y produced the zeolite-based organocatalyst. Finally, the magnetic nanoparticles (Fe_3O_4) were immobilized inside the pores of the functionalized zeolite under sonication to form the target magnetic nano-system. The magnetized structure of arginine-functionalized zeolite-NaY is identified by FT-IR, EDX-map, FE-SEM, BET, TGA–DTA XRD, TEM and VSM techniques and its catalytic activity is investigated for the synthesis of 2-amino-chromenes.

FT-IR spectra of zeolite-NaY, Pr-Cl@ZY, Arg@ZY, and Arg@ZY-Fe_3O_4 are shown in Fig. 2. In the FT-IR spectra of zeolite-NaY and the subsequent three synthetic steps, the broad bands observed in the range of 3429–3459 cm^{-1} are attributed to the stretching vibrations of hydroxyl groups of water molecules present in the zeolitic structures, while the band in the range of 1652–1635 cm^{-1} corresponds to their bending vibration. In addition, the strong and weak bands appearing at 1021–1023 cm^{-1} and 788–792 cm^{-1} are assigned to the symmetric and asymmetric stretching vibrations of Si–O–Si groups, respectively. Moreover, the band at 453 cm^{-1}, which appears with a slight shift in wavenumber, is related to the bending vibrations of Si–O–Si or Al–O–Si groups. In the FT-IR spectrum of the final step (Fig. 2d) corresponding to Arg@ZY-Fe_3O_4, weak bands are observed in the range of 1401–1650 cm^{-1}, which are most likely attributed to the vibrations of functional groups in the arginine amino acid (NH, C=N, COOH). Since the amount of arginine immobilized on the nanoporous zeolite support is small, these bands appear as weak signals or overlap with the characteristic peaks of the zeolite. Furthermore, the absorption

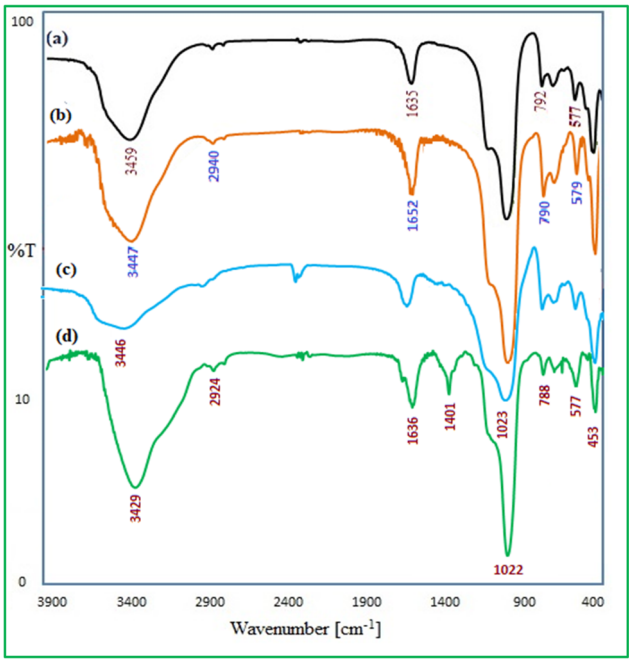

Fig. 2 Comparison of the FT-IR spectra of (a) zeolite-NaY, (b) Pr-Cl@ZY, (c) Arg@ZY and (d) Arg@ZY-Fe_3O_4.

band observed at 577 cm^{-1} in Fig. 2d is assigned to the stretching vibrations of the Fe–O bond. The presence of this band, along with the red or blue shifts of some signals compared to Fig. 2c, confirms the magnetization of the nanocomposite structure. Overall, comparison of the stepwise FT-IR spectra for the synthesis of L-Arg@ZY-Fe_3O_4 (Fig. 2) indicates the preservation of the crystalline framework of the parent zeolite despite the incorporation of functional groups.[66,67]

The morphology of zeolite-NaY, Arg@ZY, and Arg@ZY-Fe_3O_4 was analyzed using field emission scanning electron microscopy (FE-SEM) and transmission electron microscopy (TEM). As shown in Fig. 3a, pristine zeolite-NaY exhibits a well-defined crystalline structure. The images in Fig. 3b–d demonstrate that after functionalization of the zeolite with amino acid organic groups and Fe_3O_4 nanoparticles, only minor changes in the crystalline morphology are observed. These slight variations indicate the successful immobilization of organic species onto the zeolite-NaY framework, while the overall crystalline architecture of the parent zeolite remains preserved. Furthermore, the pore size was determined to be in the range of 19–40 nm, confirming the desired crystalline and mesoporous nanostructure. The TEM images (Fig. 3e and f) clearly show darker regions corresponding to Fe_3O_4 nanoparticles embedded within the lighter zeolite Y matrix. This contrast difference indicates the successful incorporation of magnetic nanoparticles into the porous structure of the zeolite rather than their mere deposition on the external surface. Considering the hierarchical pore system of zeolite Y, the Fe_3O_4 nanoparticles are likely accommodated within the larger cavities and internal channels of the zeolite framework. Such a distribution ensures strong immobilization of the magnetic phase and contributes to the observed stability and recyclability of the catalyst.

Fig. 4 illustrates the energy-dispersive X-ray (EDX) spectrum used to determine the elemental composition of Arg@ZY-Fe_3O_4 nanocatalyst surface. The spectrum confirms the presence of Na, Al, Si, O, Fe, N, and C. The Si/Al ratio in NaY zeolite was found to be 2.53, which is only slightly lower than that of the magnetic arginine-functionalized zeolite ($\approx$2.61), as reported in the quantitative results in the table of Fig. 4. This minor variation is attributed to the incorporation of silane groups during the initial modification step. Moreover, the detection of C, Fe, and N in the EDX spectrum provides clear evidence for the successful immobilization of arginine functional groups on the zeolite surface and the formation of magnetic nanoparticles within its cavities, thereby confirming the efficiency of the functionalization process.

Alongside the EDX spectrum, EDX mapping (Fig. 5) was conducted to elucidate the elemental distribution within the nanocatalyst. The mapping results clearly confirm a uniform spatial dispersion of the elements, showing strong agreement with the EDX analysis.

The Brunauer–Emmett–Teller (BET) surface area analysis is of great importance for evaluating the porosity and specific surface area of catalysts. The S_{BET} value represents the total external surface area of zeolite particles, while the internal surfaces are referred to as pores. Table 1 summarizes the structural data of the zeolite–arginine nanocomposite obtained from the porosity analysis. According to the results, the S_{BET} value of pure zeolite was measured to be 441 $m^2\ g^{-1}$, whereas that of the final nanocatalyst (Arg@ZY-Fe_3O_4) was 127 $m^2\ g^{-1}$. The significant reduction in surface area not only confirms the successful functionalization process of the zeolite structure but also indicates the partial pore filling by organic functional groups.

Fig. 6 presents the nitrogen adsorption–desorption isotherms of the arginine-modified zeolite/Fe_3O_4 catalyst and the pristine zeolite at constant temperature, providing further confirmation of the successful synthesis. The isotherm of the pure zeolite follows a type I pattern, characteristic of microporous materials with pore diameters smaller than 2 nm. In contrast, the nanocatalyst Arg@zeolite-Y exhibits a type IV isotherm with a small hysteresis loop. According to the IUPAC classification, this hysteresis corresponds to the H1 type and appears within the relative pressure range of $P/P_0 = 0.4–0.9$. The presence of a hysteresis loop in an isotherm is indicative of mesopores (2–50 nm), and its shape compared with reference profiles provides insight into the geometry of the internal pores. Examination of the isotherm of the final nanocomposite clearly reveals that anchoring arginine functional groups induces a layered structure with abundant pores on the zeolite surface.[68–70] Furthermore, the pore size distribution analysis indicates that most pores fall within the range of 2–46 nm, and the distribution profile confirms the presence of three categories of pores – small, medium, and large – which are characteristic of Y-type zeolites.

The TGA analysis of the synthesized nanocomposite showed distinct thermal decomposition steps (Fig. 7). An initial weight loss of 7.50% below 150 °C was attributed to the removal of physically adsorbed water and surface moisture. A major weight

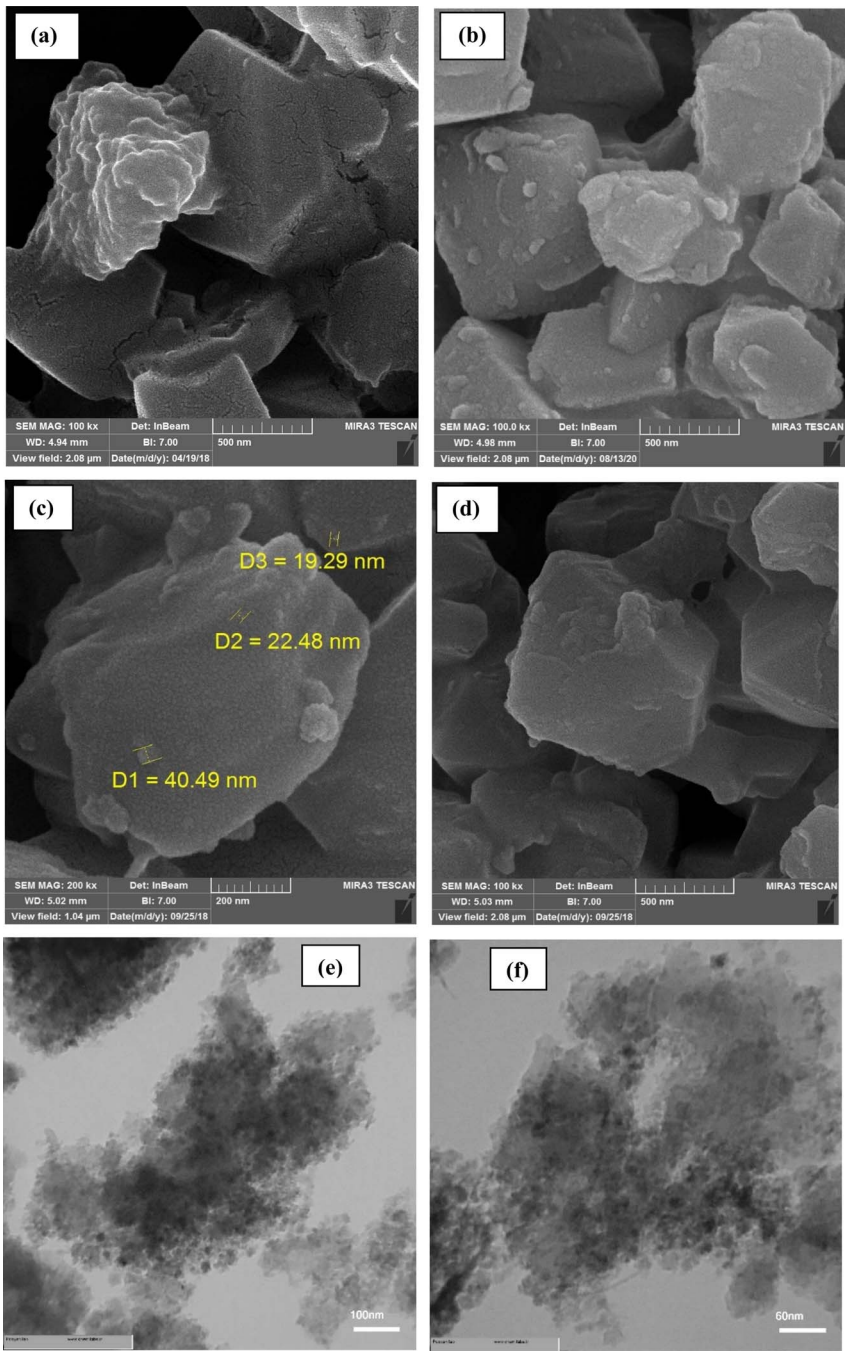

Fig. 3 FE-SEM images of (a) zeolite-NaY, (b) Arg@ZY, (c and d) Arg@ZY-Fe_3O_4 and (e and f) the TEM images.

reduction occurred in the range of 200–575 °C, corresponding to the gradual decomposition of the immobilized amino acid on the magnetic zeolite support. In this stage, a total weight loss of about 25.29% (equivalent to 1.041 mg) was recorded, confirming the effective loading of the organic moiety onto the inorganic matrix. The overall stability of the mineral structure up to nearly 700 °C highlights the excellent thermal resistance of the nanocomposite, supporting its potential as a robust hybrid platform for catalytic and environmental applications.

The X-ray diffraction (XRD) patterns of pure zeolite, the Arg@ZY nanocomposite, and the magnetic nanocatalyst Arg@ZY-Fe_3O_4 are presented in Fig. 8. The XRD pattern of zeolite-Y exhibits a complete match with the faujasite structure (JCPDS card no. 39-1380), confirming its crystalline nature. The diffraction pattern of the Arg@ZY nanocomposite is also highly similar to that of zeolite-NaY, indicating that the zeolite framework remained intact after the modification process. It is observed that the immobilization of arginine on the zeolite surface caused slight variations in the intensity and position of certain peaks; however, no distinct new signals attributable to arginine appeared. This phenomenon is most likely due to the relatively low content of the amino acid within the organo-

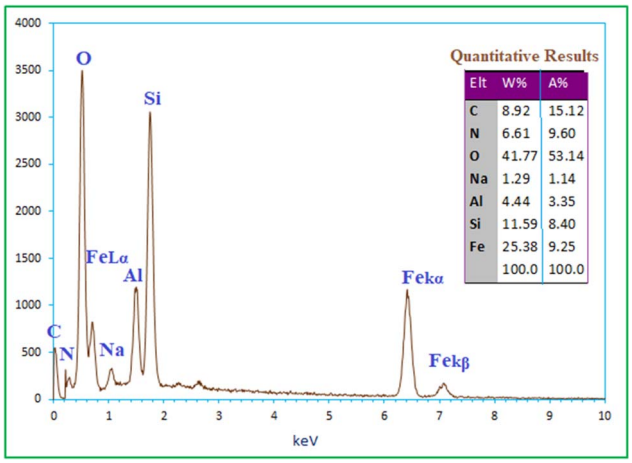

Fig. 4 Energy dispersive X-ray (EDX-map) analysis of the Arg@ZY-Fe_3O_4 nanocomposite.

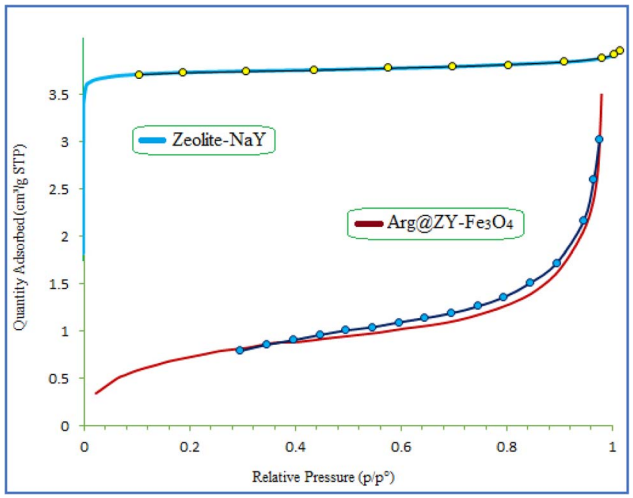

Fig. 6 Adsorption–desorption isotherm curves for samples zeolite NaY and Arg@ZY-Fe_3O_4.

zeolite structure.[71,72] In the final Arg@ZY-Fe_3O_4 magnetic structure, as expected, in addition to the characteristic peaks of zeolite, the typical diffraction peaks of magnetic Fe_3O_4 nanoparticles were also observed. The diffraction pattern exhibited 2θ values and indices at 6.16° (111), 10.28° (220), 11.80° (311), 15.72° (331), 18.68° (440), 20.52° (551), 23.68° (553), 31.44° (555), and 35.16° (840), corresponding to zeolite-NaY crystals. Furthermore, as shown in Fig. 8, significant new peaks were detected at 30.80° (220), 35.88° (331), 43.52° (400), 52.48° (442), 57.32° (511), 63.10° (440), and 73.16° (533), which are attributed to cubic iron oxide (Fe_3O_4) nanoparticles.[73] These results demonstrate that the zeolite-NaY framework was preserved after modification. Based on the Debye–Scherrer equation, the average crystallite sizes were calculated to be approximately 27.04 nm for Fe_3O_4 nanoparticles and 44.68 nm for zeolite-Y.

As illustrated in Fig. 9, vibrating sample magnetometry (VSM) was employed to assess the magnetic properties of

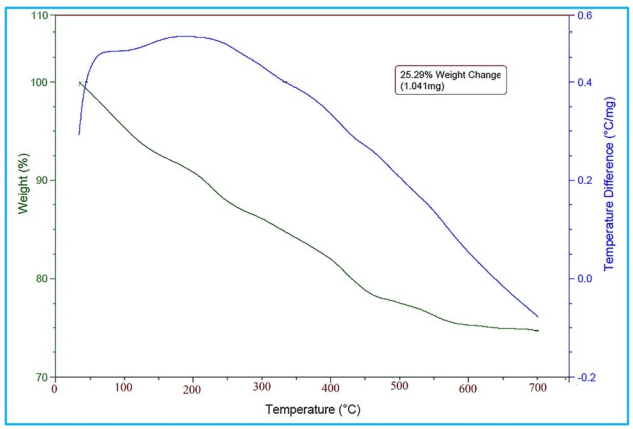

Fig. 7 TGA–DTG curves of the Arg@ZY-Fe_3O_4 nanocomposite.

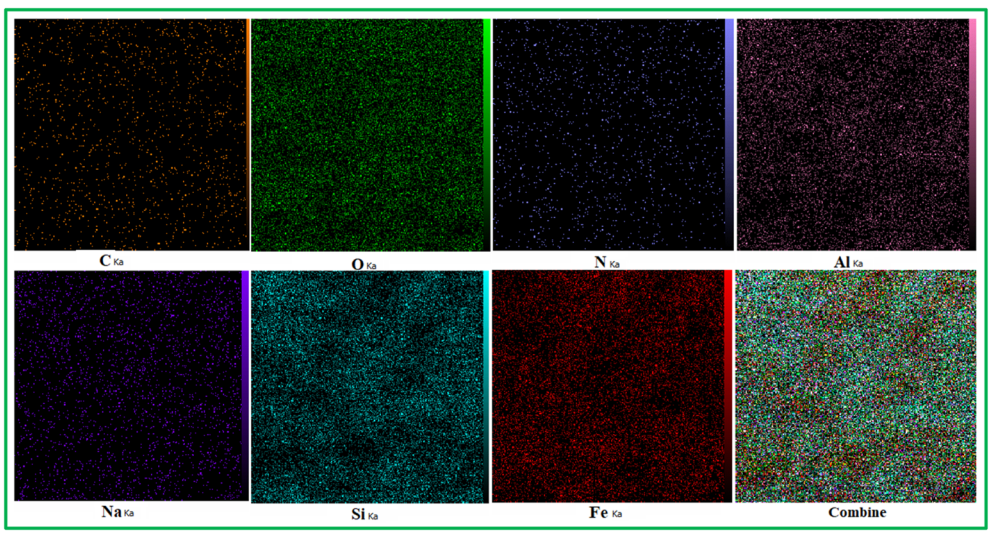

Fig. 5 Elemental distribution map (EDX-map) of elements in the Arg@ZY-Fe_3O_4.

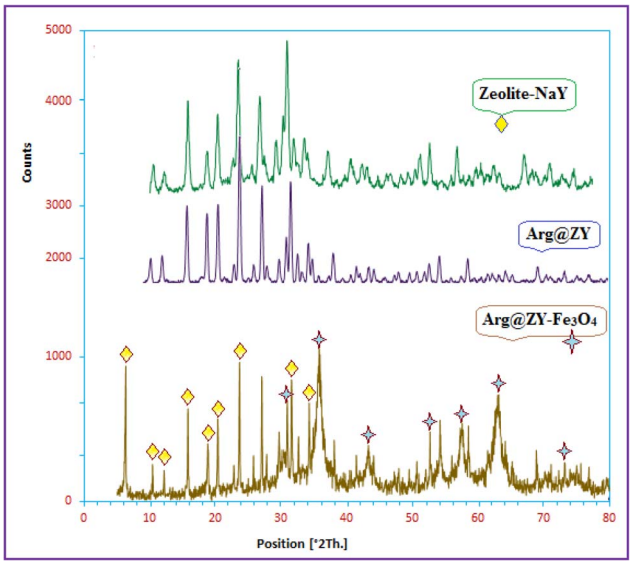

Fig. 8 XRD spectrum of zeolite-NaY, Arg@ZY and Arg@ZY-Fe_3O_4 nanocomposite.

Arg@ZY-Fe_3O_4. The analysis revealed a saturation magnetization of 27.79 emu g^{-1} for the composite. Although the incorporation of Fe_3O_4 nanoparticles into the zeolite framework *via* the core–shell approach led to a reduction in magnetic strength compared to pure Fe_3O_4, the resulting magnetization remains sufficient to enable facile recovery and separation of the catalyst from the reaction medium using an external magnetic field.

3.2. Investigation of catalyst activity

To evaluate the catalytic performance of Arg@ZY-Fe_3O_4 nanocomposite in the synthesis of 2-aminochromene derivatives, optimization of the reaction conditions was carried out. For this purpose, the reaction of benzaldehyde, malononitrile, and resorcinol was selected as a model reaction, and the results are summarized in Table 2. Based on previous reports and preliminary experiments, the reaction was initially performed using 10 wt% of the catalyst (14 mg) in ethanol as a green solvent at room temperature. An increase in temperature led to a higher reaction yield. Furthermore, when a water–ethanol mixture was used as the solvent, both the reaction yield and rate were significantly improved (entry 4, Table 2). Subsequently, the influence of solvent type, reaction temperature, and catalyst loading was systematically investigated to determine the optimal conditions. The results indicated that at 90 °C with 10 wt% catalyst, water acted as the most efficient solvent, affording the desired product in 97% yield within 5 minutes (entry 6, Table 2). Control experiments revealed that in the absence of the catalyst or in the presence of individual components such as NaY zeolite, L-arginine, or Fe_3O_4 nanoparticles, the reaction did not proceed efficiently. Moreover, performing the reaction under solvent-free conditions at 90 °C also resulted in poor conversion. Overall, the findings demonstrate that the Arg@ZY-Fe_3O_4 nanocatalyst, containing organic amino acid functional groups supported on a magnetic zeolite framework, exhibits superior catalytic activity compared to each of its individual components and can serve as an efficient and recyclable catalyst for the synthesis of 2-aminochromenes.

After optimization of the reaction conditions for the model reaction, the efficiency and general applicability of the developed protocol were further examined through a series of three-component reactions. Under the optimized conditions,

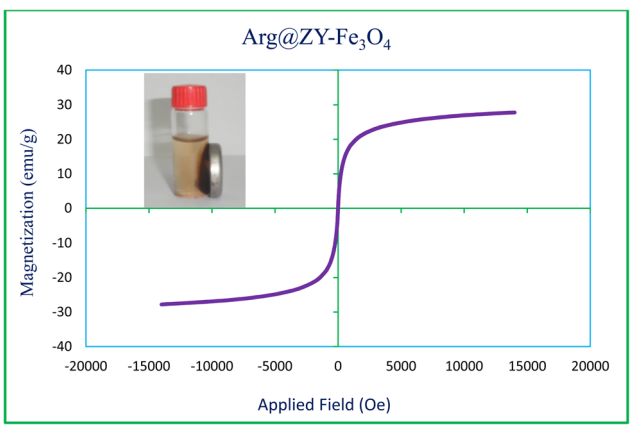

Fig. 9 Field-dependent magnetization curve measured for Arg@ZY-Fe_3O_4 nanocomposite.

Table 2 Optimizing the reaction conditions for synthesis of 2-amino-7-hydroxy-4-phenyl-4*H*-chromene-3-carbonitrile using Arg@ZY-Fe_3O_4 nanocatalyst[a]

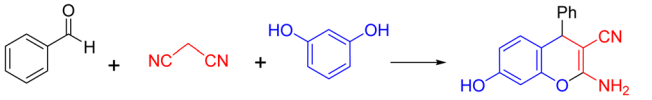

Entry	Catalyst loading, (wt/wt%)	Solvent	Temperature (°C)	Time (min)	Yield[b] (%)
1	—	Ethanol	80	24 h	—
2	10	Ethanol	25	60	25
3	10	Ethanol	80	20	88
4	10	H_2O/EtOH (1 : 1 ratio)	80	16	90
5	10	H_2O	80	10	92
6	**10**	**H_2O**	**90**	**5**	**97**
7	10	H_2O	100	5	97
8	10	H_2O	25	60	55
9	15	H_2O	90	4	97
10	5	H_2O	90	15	65
11	10	CH_3OH	80	15	73
12	10	CH_3–CN	80	20	65
13	10	CH_2Cl_2	40	30	10
14	—	H_2O	90	30	30
15	10	—	90	20	65
16	10 (zeolite-NaY)	H_2O	90	30	20
17	10 (L-arginine)	H_2O	90	15	30
18	10 (Arg@ZY)	H_2O	90	8	89
19	10 (Fe_3O_4)	H_2O	90	15	25

[a] Reaction condition: resorcinol (1 mmol), benzaldehyde (1 mmol) and malononitrile (1 mmol). [b] Isolated yield.

Table 3 Synthesis of 4*H*-pyran and -chromene derivatives **6a–i**, **7a–f** and **8a–f** catalyzed by Arg@ZY-Fe_3O_4 under the optimized reaction conditions[a]

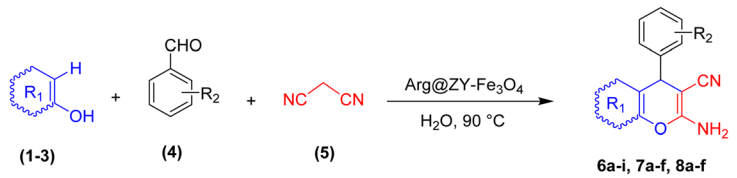

Entry	R_1	R_2	Product	Time (min)	Yield[a] (%)	M.p. (°C) (lit.)	AEf[b] (%)/*E*-factor
1	Resorcinol	H	**6a**	5	97	238–239 (230–231)[52]	93.6/0.07
2	Resorcinol	4-Cl	**6b**	7	93	155–156 (160–162)[52]	93.6/0.07
3	Resorcinol	2,4-Cl	**6c**	9	91	252–254 (257–259)[46]	93.6/0.08
4	Resorcinol	2-NO_2	**6d**	7	92	176–178 (160–162)[46]	93.6/0.07
5	Resorcinol	3-NO_2	**6e**	8	95	174–176 (170–172)[55]	93.6/0.07
6	Resorcinol	4-NO_2	**6f**	5	99	165–167 (168–170)[46]	93.6/0.07
7	Resorcinol	4-CH_3	**6g**	12	91	188–190 (182–183)[52]	93.6/0.08
8	Resorcinol	4-OCH_3	**6h**	14	90	190–192 (111–113)[52]	93.6/0.08
9	Resorcinol	3,4-OCH_3	**6i**	12	88	152–154 (148–150)[61]	93.6/0.08
10	Dimedone	H	**7a**	7	95	227–229 (230–231)[55]	94.2/0.06
11	Dimedone	2-Cl	**7b**	9	93	192–194 (195–197)[55]	94.2/0.07
12	Dimedone	2,4-Cl	**7c**	10	95	192–194 (190–191)[55]	94.2/0.06
13	Dimedone	2-NO_2	**7d**	7	96	241–243 (230–232)[54]	94.2/0.06
14	Dimedone	4-NO_2	**7e**	5	99	190–191 (178–180)[54]	94.2/0.06
15	Dimedone	4-OCH_3	**7f**	12	91	188–190 (201–203)[55]	94.2/0.07
16	2-Naphthol	H	**8a**	12	90	287–289 (281–283)[61]	94.3/0.07
17	2-Naphthol	2-Cl	**8b**	11	92	266–268 (270–271)[55]	94.3/0.07
18	2-Naphthol	3-NO_2	**8c**	10	92	238–240 (238–240)[55]	94.3/0.07
19	2-Naphthol	4-NO_2	**8d**	9	97	186–188 (184–185)[55]	94.3/0.06
20	2-Naphthol	4-OCH_3	**8e**	14	89	171–173 (188–189)[55]	94.3/0.07
21	2-Naphthol	3,4-OCH_3	**8f**	11	90	187–189 (195–196)[62]	94.3/0.07

[a] Pure product isolated. [b] Atom economy of efficiency.

malononitrile, resorcinol, 2-naphthol, or dimedone were reacted with various aryl aldehydes bearing electron-donating and electron-withdrawing substituents to afford a wide range of substituted 2-aminochromene derivatives. This methodology was successfully applied to the synthesis of 2-amino-4-aryl-7-hydroxy-4*H*-chromene-3-carbonitriles, 3-amino-1-aryl-1*H*-benzo[*f*]chromene-2-carbonitriles, and 2-amino-5-oxo-5,6,7,8-tetrahydro-4*H*-benzo[*b*]pyrans. All the desired products were obtained in good to excellent yields, and the corresponding results are summarized in Table 3.

In addition, the calculated atom economy[74] and *E*-factor[75] values demonstrate that all reactions exhibit excellent atom efficiency, with atom economy values ranging from 93.6 to 94.3% (Table 3) These high values indicate that most of the atoms from the starting materials are efficiently incorporated into the final products, while only a minimal amount of waste in the form of water is generated as a byproduct. Moreover, the very low *E*-factor values (0.06–0.08) reflect negligible waste production, which is consistent with the high reaction yields and the use of recyclable water as a green solvent. Overall, these results confirm the environmentally benign, sustainable, and green nature of the developed synthetic protocol.

The plausible reaction mechanism for the catalytic synthesis of functionalized chromenes is illustrated in Scheme 3. The Arg@ZY-Fe_3O_4 nanocatalyst can act as a multifunctional catalyst owing to the presence of both Brønsted and Lewis acidic sites (–COOH and Fe_3O_4) as well as Brønsted basic sites (–NH_2). The amino acid moieties and Fe_3O_4 nanoparticles serve as Brønsted and Lewis acids, respectively, to activate the carbonyl group of the aromatic aldehyde (**1**). Subsequently, a Knoevenagel condensation with malononitrile (**2**) affords the intermediate (**A**). The Lewis acidic or Brønsted basic centers of Fe_3O_4 or arginine promote the formation of the enolic form of phenols or dimedone (**3**). The enol form of compound (**3**) then undergoes a Michael addition with the activated alkene (**A**) to generate intermediate (**B**). This intermediate (**B**) undergoes intramolecular cyclization through nucleophilic attack of the phenoxide ion on the nitrile (–CN) group to form intermediate (**C**), which is finally tautomerized in the presence of the Arg@ZY-Fe_3O_4 nanocatalyst to yield the desired 2-amino-chromene derivatives (**4**, **6**, and **8**).

To confirm the heterogeneous nature of the catalyst, a hot filtration test was carried out. The model reaction was interrupted after approximately 2.5 min (corresponding to about 50% of the total reaction time), and the magnetic L-Arg@ZY-Fe_3O_4 nanocatalyst was removed from the reaction mixture under hot conditions using an external magnet. The reaction mixture was then allowed to continue for the remaining

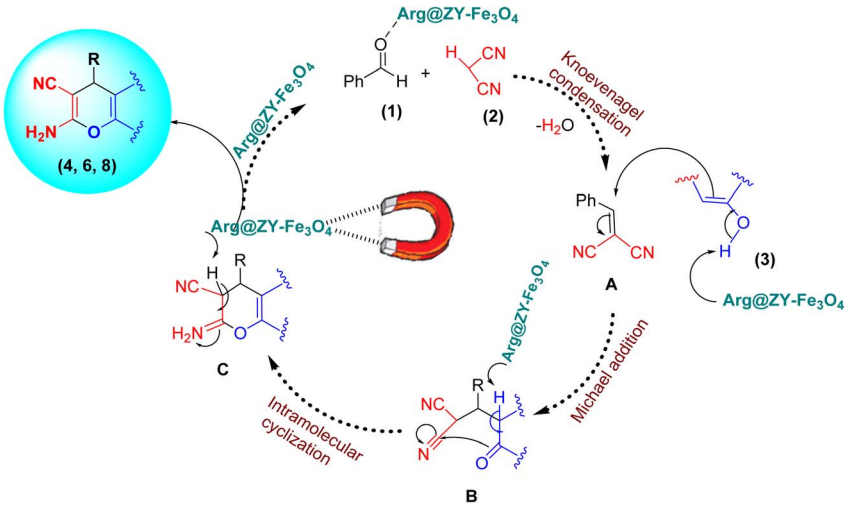

Scheme 3 Proposed mechanism pathway for the synthesis of 2-amino-4*H*-chromenes using Arg@ZY-Fe_3O_4.

Table 4 Comparison of the synthesis of compounds **6a**, **7a** and **8a** using the Arg@ZY-Fe_3O_4 catalyst with other reported methods

Product	Catalyst	Conditions	Time (min)	Yield (%)
6a	K_2CO_3 (1 mmol)	MDW[a], 70 °C	240	96 (ref. 46)
6a	Zn(L-proline)$_2$ (20 mol%)	EtOH/H_2O, reflux	240	89 (ref. 55)
6a	Nano-cellulose-OTiCl_3 (3 mg)	EtOH, reflux	20	94 (ref. 52)
6a	Triethanolamine (30 mol%)	H_2O, reflux	45	92 (ref. 53)
6a	Arg@ZY-Fe_3O_4 (10 wt%)	H_2O, 90 °C	5	97 (this work)
7a	Picolinic acid (15 mol%)	EtOH/H_2O, 60 °C	10	98 (ref. 54)
7a	Piperazine-GO (1 mol%)	EtOH/H_2O, 50 °C	15	95 (ref. 61)
7a	$Na_3[CrMo_6O_{24}H_6]\cdot 8H_2O$@$ZrO_2$ (20 mg)	EtOH, reflux	10	98 (ref. 44)
7a	Talc (0.06 g)	Solvent-free, 90 °C	35	90 (ref. 60)
7a	Arg@ZY-Fe_3O_4 (10 wt%)	H_2O, 90 °C	7	95 (this work)
8a	Talc (0.06 g)	Solvent-free, 90 °C	40	91 (ref. 60)
8a	Piperidine (0.5 mL)	MW, 140 °C	2	87 (ref. 62)
8a	Zn(L-proline)$_2$ (20 mol%)	EtOH/H_2O, reflux	240	90 (ref. 55)
8a	Piperazine-GO (3 mol%)	Solvent-free, 100 °C	40	97 (ref. 61)
8a	Arg@ZY-Fe_3O_4 (10 wt%)	H_2O, 90 °C	12	90 (this work)

[a] Magnetized distilled water.

reaction time in the absence of the catalyst. TLC monitoring revealed no further progress of the reaction, and unreacted starting materials were still present. In contrast, when the same reaction was allowed to proceed in the presence of the catalyst for the full reaction time at 90 °C, the desired product was obtained in high yield. These observations clearly indicate that no catalytically active species leached into the reaction medium and that the catalytic activity originates exclusively from the solid catalyst, thus confirming the truly heterogeneous nature of the L-Arg@ZY-Fe_3O_4 nanocatalyst.

Subsequently, a comprehensive comparison was carried out between the optimized reaction conditions developed in this study for the synthesis of 4*H*-pyran and chromene derivatives and those reported in previous studies, as summarized in Table 4. Table 4 outlines the various reaction conditions employed in earlier works, including the type of catalyst, solvent, reaction temperature, and reaction time. This comparison clearly highlights the efficiency and advantages of the proposed methodology, demonstrating its superior performance in terms of higher yields, improved selectivity, and milder reaction conditions compared to previously reported methods.

The reusability of the Arg@ZY-Fe_3O_4 organocatalyst was evaluated as shown in Fig. 10 using the model reaction under optimized conditions. After the catalytic process is complete, the nanocatalyst is separated from the reaction vessel with the help of a magnet, washed several times with water and ethanol, then dried and reused for the next reaction. The Arg@ZY-Fe_3O_4 catalyst can be reused more than five consecutive cycles without any significant decrease about catalytic activity.

The FT-IR spectroscopy results also confirmed that the fundamental structure of the reused catalyst remained intact. As shown in Fig. 11, the FT-IR spectra of the recovered and fresh zeolitic catalysts are essentially identical, exhibiting no significant differences.

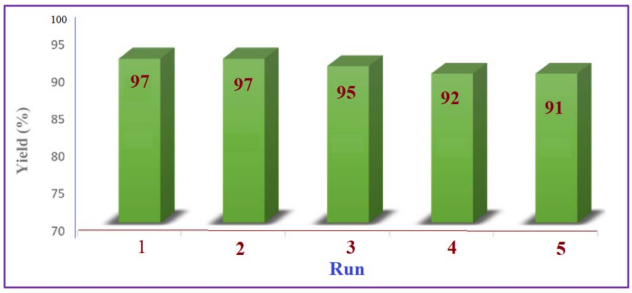

Fig. 10 Reusability of Arg@ZY-Fe_3O_4 using the model reaction.

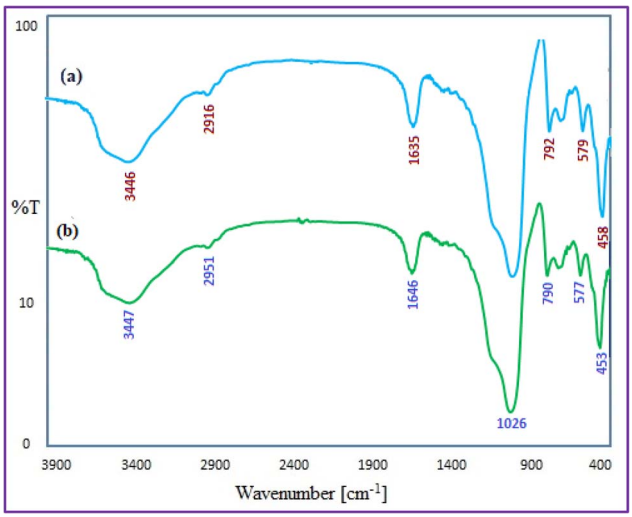

Fig. 11 FT-IR spectrum of recovered Arg@ZY-Fe_3O_4 (a) after the 5 cycle and the fresh nanocatalyst (b).

4. Conclusion

In conclusion, in this study, a novel magnetic zeolitic nanostructure functionalized with the amino acid arginine was successfully designed and synthesized. The resulting hybrid zeolitic material possesses abundant N-basic sites along with Brønsted and Lewis acid sites, enabling its application as an efficient multifunctional magnetic nanocatalyst for the green, three-component synthesis of 2-aminochromenes in aqueous media. The obtained results demonstrated that the Arg@ZY-Fe_3O_4 organocatalyst exhibits excellent stability, good reusability, and remarkable catalytic activity. Therefore, this magnetic organocatalyst is expected to hold great potential for future applications in environmentally benign acid–base catalyzed liquid-phase reactions and the sustainable synthesis of valuable heterocyclic compounds.

Author contributions

Definition, supervision, reviewing, editing, initial writing, drawing of figures and interpretation of nanocatalyst identification analyzes [Mehdi Kalhor]. The fabrication of nano catalyst, experiments and synthesis of the target heterocycles [Samira Zebardast]. All authors read and approved the final manuscript.

Conflicts of interest

The authors declare that they have no interest to influence the work reported in this paper.

Data availability

The spectral data which could be supported our findings are available as supplementary information (SI) attached to this article. Supplementary information is available. See DOI: https://doi.org/10.1039/d5na01102g.

Acknowledgements

We are grateful to the research commute of Payame Noor University for providing financial and technical supports for this work.

References

1 F. Sher, I. Ziani, M. Hameed, S. Ali and J. Sulejmanović, *Curr. Opin. Green Sustainable Chem.*, 2024, **47**, 100925, DOI: 10.1016/j.cogsc.2024.100925.
2 R. O. Afolabi, *J. Mol. Liq.*, 2024, **397**, 124190, DOI: 10.1016/j.molliq.2024.124190.
3 I. Ahmad, M. A. Aftab, A. Fatima, S. D. Mekkey, S. Melhi and S. Ikram, *Coord. Chem. Rev.*, 2024, **514**, 215904, DOI: 10.1016/j.ccr.2024.215904.
4 D. N. Gaikwad, S. T. Gaikwad, R. K. Manjul, A. S. Rajbhoj, D. M. Suryavanshi, G. A. Varade and N. S. Dhane, *Lett. Org. Chem.*, 2025, **22**, 102–115, DOI: 10.2174/0115701786307065240527172814.
5 M. R. Das, N. Hussain, R. Duarah, N. Sharma, P. Sarmah, A. Thakur, P. Bhattacharjee, U. Bora and R. Boukherroub, *Catal. Rev.*, 2022, **66**, 923–995, DOI: 10.1080/01614940.2022.2100633.
6 F. Sher, I. Ziani, M. Hameed, S. Ali and J. Sulejmanović, *Curr. Opin. Green Sustainable Chem.*, 2024, **47**, 100925, DOI: 10.1016/j.cogsc.2024.100925.
7 Ü. Y. Yıldız, R. Keçili and C. M. Hussain, Green and sustainable chemistry, *Green Imprinted Materials*, Elsevier, 2024, ch. 1, pp. 3–25, DOI: 10.1016/B978-0-443-15431-7.00014-3.
8 D. Jagadeesan, *Appl. Catal., A*, 2016, **511**, 59–77, DOI: 10.1016/j.apcata.2015.11.033.
9 M. Kalhor, Z. Vahedi and H. Gharoubi, *RSC Adv.*, 2023, **13**, 9208–9221, DOI: 10.1039/D3RA00758H.
10 C. Srilakshmi and R. Saraf, *ACS Omega*, 2018, **3**, 10503–10512, DOI: 10.1021/acsomega.8b01255.
11 M. Kalhor, M. Bigdeli and H. Moghanian, *Res. Chem. Intermed.*, 2023, **49**, 5375–5394, DOI: 10.1007/s11164-023-05146-9.

12 N. Salleh, M. M. Mahat, S. M. Yahaya and R. Ramli, *J. Adv. Res. Micro Nano Eng.*, 2024, **18**, 32–43, DOI: 10.37934/armne.18.1.3243.
13 M. Al-Samhan and J. Al-Fadhli, *Catal. Lett.*, 2024, **154**, 4719–4728, DOI: 10.1007/s10562-024-04635-9.
14 Y. Wang, X. Ma, H. Wang, D. Zhao, Y. Liu and Z. Ma, *Molecules*, 2024, **29**, 3507, DOI: 10.3390/molecules29153507.
15 B. Muir, M. Wołowiec, T. Bajda, P. Nowak and P. Czupryński, *Mineralogia*, 2017, **48**, 145–156, DOI: 10.1515/mipo-2017-0017.
16 A. Ehsani, M. K. Moftakhar and M. Kalhor, *J. Energy Storage*, 2022, **55**, 105489, DOI: 10.1016/j.est.2022.105489.
17 M. Kalhor, S. Banibairami and S. A. Mirshokraie, *Green Chem. Lett. Rev.*, 2018, **11**, 334–344, DOI: 10.1080/17518253.2018.1499968.
18 T. Vangijzegem, V. Lecomte, I. Ternad, L. V. Leuven, R. N. Muller, D. Stanicki and S. Laurent, *Pharmaceutics*, 2023, **15**, 236, DOI: 10.3390/pharmaceutics15010236.
19 H. Veisi, M. Pirhayati, P. Mohammadi, T. Tamoradi, S. Hemmati and B. Karmakar, *RSC Adv.*, 2023, **13**, 20530–20556, DOI: 10.1039/D3RA01208E.
20 S. Sharma, H. Sharma and R. Sharma, *Chem. Inorg. Mater.*, 2024, **2**, 100035, DOI: 10.1016/j.cinorg.2024.100035.
21 A. Hu, G. T. Yee and W. Lin, *J. Am. Chem. Soc.*, 2005, **127**, 12486–12487, DOI: 10.1021/ja053881o.
22 Y. Zhang, W. Li, J. Wang, J. Jin, Y. Zhang, J. Cheng and Q. Zhang, *Front. Chem.*, 2023, **10**, 1106426, DOI: 10.3389/fchem.2022.1106426.
23 P. Rai and D. Gupta, *Synth. Commun.*, 2021, **51**, 3059–3083, DOI: 10.1080/00397911.2021.1968910.
24 Y. A. Fahim, I. W. Hasani and W. Mahmoud Ragab, *Eur. J. Med. Res.*, 2025, **30**, 441, DOI: 10.1186/s40001-025-02696-z.
25 Z. Birch-Price, F. J. Hardy, T. M. Lister, A. R. Kohn and A. P. Green, *Chem. Rev.*, 2024, **124**, 8740–8786, DOI: 10.1021/acs.chemrev.4c00120.
26 K. Kamanna, *Curr. Organocatal.*, 2021, **8**, 126–146, DOI: 10.2174/2213337207999201117093848.
27 Z. Chaia and G. Zhao, *Catal. Sci. Technol.*, 2012, **2**, 29–41, DOI: 10.1039/C1CY00347J.
28 F. Werlinger, M. Beroíza-Duhart, O. A. Douglas-Gallardo, S. Oyarzo-Aro, M. L. Valenzuela, O. S. Trofymchuk, M. E. Flores and J. Martínez, *Org. Biomol. Chem.*, 2024, **22**, 4135–4144, DOI: 10.1039/D4OB00339J.
29 J. Paradowska, M. Stodulski and J. Mlynarski, *Angew. Chem.*, 2009, **48**, 4288–4297, DOI: 10.1002/anie.200802038.
30 S. Malhotra, D. Jaspal and A. Malviya, *Arabian J. Chem.*, 2019, **12**, 1247–1251, DOI: 10.1016/j.arabjc.2014.10.048.
31 Z. Heidarnezhad, A. Ghorbani-Choghamarani and Z. Taherinia, *Nanoscale Adv.*, 2024, **6**, 2431–2446, DOI: 10.1039/D3NA00318C.
32 S. Rostamnia and E. Doustkhah, *RSC Adv.*, 2014, **4**, 28238–28248, DOI: 10.1039/C4RA03773A.
33 O. Sánchez-Antonio, K. A. Romero-Sedglach, E. C. Vázquez-Orta and E. Juaristi, *Molecules*, 2020, **25**, 4532, DOI: 10.3390/molecules25194532.
34 A. Erigoni and U. Diaz, *Catalysts*, 2021, **11**, 79, DOI: 10.3390/catal11010079.
35 F. Bijari, M. Talebi, H. Ghafuri, Z. Tajik and P. Hanifehnejad, *Chem. Proc.*, 2022, **12**, 50, DOI: 10.3390/ecsoc-26-13708.
36 G. Fu, Q. Zhang, J. Wu, D. Sun, L. Xu, Y. Tang and Y. Chen, *Nano Res.*, 2015, **8**, 3963–3971, DOI: 10.1007/s12274-015-0899-3.
37 K. Azizi, M. Karimi, H. R. Shaterian and A. Heydari, *RSC Adv.*, 2014, **4**, 42220–42225, DOI: 10.1039/C4RA06198E.
38 H. S. Ali and S. P. de Visser, *Front. Chem.*, 2024, **12**, 1–14, DOI: 10.3389/fchem.2024.1365494.
39 M. Kalhor, Z. Modares and V. Azizkhani, *RSC Adv.*, 2025, **15**, 28045–28062, DOI: 10.1039/d5ra04062k.
40 V. Raj and J. Lee, *Front. Chem.*, 2020, **8**, 623, DOI: 10.3389/fchem.2020.00623.
41 M. K. Katiyar, G. K. Dhakad, B. Shivani, S. Arora, S. Bhagat, T. Arora and R. Kumar, *J. Mol. Struct.*, 2022, **1263**, 133012, DOI: 10.1016/j.molstruc.2022.133012.
42 M. Azimi, Z. Najafi, A. Bahmani, G. Chehardoli and A. Iraji, *BMC Chem.*, 2024, **18**, 187, DOI: 10.1186/s13065-024-01305-0.
43 G. P. Ellis, *The Chemistry of Heterocyclic Compounds: Chromenes, Chromanones, and Chromones*, ed. A. Weissberger and E. C. Taylor, John Wiley, New York, NY, USA, 1977, vol. 31, pp. 1–1085, ISBN: 0-471-38212-4.
44 P. Kadam, S. Bubanale, S. Sabale, S. Maradur and A. Supale, *React. Kinet., Mech. Catal.*, 2025, **138**, 873–888, DOI: 10.1007/s11144-024-02762-3.
45 G. G. El-Bana, M. A. Salem, M. H. Helal, O. Alharbi and M. A. Gouda, *Mini-Rev. Org. Chem.*, 2024, **21**, 73–91, DOI: 10.2174/1570193X19666220527163846.
46 M. Bakherad, A. Keivanloo, H. Rezaei and A. Rezaeifard, *Iran. J. Chem. Chem. Eng.*, 2023, **41**, 853–862, DOI: 10.30492/ijcce.2022.548084.5172.
47 Z. Wen, K. C. Yang, J. F. Deng and L. Chen, *Adv. Synth. Catal.*, 2023, **365**, 1290–1331, DOI: 10.1002/adsc.202201409.
48 K. N. Sharon, P. Padmaja and P. N. Reddy, *ChemistrySelect*, 2024, **9**, e202400565, DOI: 10.1002/slct.202400565.
49 S. Samai, S. Atta and M. S. Singh, *ChemistrySelect*, 2025, **10**, e01023, DOI: 10.1002/slct.202501023.
50 A. Thakral, M. Verma, A. Thakur, R. Bharti and R. Sharma, *Polycyclic Aromat. Compd.*, 2023, **44**, 1697–1721, DOI: 10.1080/10406638.2023.2203506.
51 M. Chadha, A. Garg, A. Bhalla and S. Berry, *Tetrahedron*, 2024, **150**, 133741, DOI: 10.1016/j.tet.2023.133741.
52 B. Sadeghi, E. Arabian and E. Akbarzadeh, *Inorg. Nano-Met. Chem.*, 2020, **50**, 1207–1212, DOI: 10.1080/24701556.2020.1739076.
53 F. Mohamadpour, *Sustainable Chem. Environ.*, 2025, **11**, 100279, DOI: 10.1016/j.scenv.2025.100279.
54 S. D. Vankar, H. M. Makwana and M. G. Sharma, *RSC Adv.*, 2025, **15**, 19069–19078, DOI: 10.1039/D5RA02718G.
55 D. Tahmassebi, J. E. Blevins and S. S. Gerardot, *Appl. Organomet. Chem.*, 2019, **33**, e4807, DOI: 10.1002/aoc.4807.
56 M. Kamalzare, M. Bayat and A. Maleki, *R. Soc. Open Sci.*, 2020, **7**, 200385, DOI: 10.1098/rsos.200385.
57 A. M. Fouda, A. Irfan, A. G. Al-Sehemi and A. M. El-Agrody, *J. Mol. Struct.*, 2021, **1240**, 130542, DOI: 10.1016/j.molstruc.2021.130542.

58 M. El Gaafary, J. Lehner, A. M. Fouda, A. Hamed, J. Ulrich, T. Simmet, T. Syrovets and A. M. El-Agrody, *Bioorg. Chem.*, 2021, **116**, 105402, DOI: 10.1016/j.bioorg.2021.105402.
59 P. Pérez-Ramos, G. Biniari, R. G. Soengas, H. Rodríguez-Solla and C. Simal, *Chem.–Eur. J.*, 2025, **31**, e202500283, DOI: 10.1002/chem.202500283.
60 M. Hajihasani Bafghi, A. Bamoniri and B. B. F. Mirjalili, *Sci. Rep.*, 2025, **15**, 14167, DOI: 10.1038/s41598-025-95727-y.
61 A. Khazaee, R. Jahanshahi, S. Sobhani, J. Skibsted and J. M. Sansano, *Green Chem.*, 2020, **22**, 4604–4616, DOI: 10.1039/D0GC01274B.
62 H. M. Mohamed, A. M. Fouda, E. Khattab, A. M. Agrody and T. H. Afifi, *Z. Naturforsch., C: J. Biosci.*, 2017, **72**, 161–171, DOI: 10.1515/znc-2016-0139.
63 N. Hassanzadeh, M. G. Dekamin and E. Valiey, *Nanoscale Adv.*, 2025, **7**, 99–123, DOI: 10.1039/D4NA00264D.
64 M. Kalhor, P. Nozare, E. Vessally and B. Mohammadi, *ChemistrySelect*, 2023, **8**, e202301283, DOI: 10.1002/slct.202301283.
65 M. Kalhor and Z. Zarnegar, *RSC Adv.*, 2019, **9**, 19333–19346, DOI: 10.1039/C9RA02910A.
66 B. Lesiak, L. Kövér, J. Tóth, A. Jablonski, J. Zemek, P. Jiricek, A. Kromka and N. Rangam, *Front. Chem.*, 2019, **7**, 642, DOI: 10.3389/fchem.2019.00642.
67 J. Perez-Pariente, J. A. Martens and P. A. Jacobs, *Appl. Catal.*, 1987, **31**, 35–64, DOI: 10.1016/S0166-9834(00)80665-X.
68 P. Li, Y. Wang, H. Li and G. Calzaferri, *Angew. Chem., Int. Ed.*, 2014, **53**, 2904–2909, DOI: 10.1002/anie.201310485.
69 E. Pérez-Botella, J. García-Martínez, H. Fridmann and J. L. Jordá, *Chem. Rev.*, 2022, **122**, 785–858, DOI: 10.1021/acs.chemrev.2c00140.
70 Y.-S. Bae, A. Ö. Yazaydin and R. Q. Snurr, *Langmuir*, 2010, **26**, 5475–5483, DOI: 10.1021/la100449z.
71 P. S. Endang, A. R. Rahadian, T. I. M. Ulva, R. W. Alvin, M. I. Rendy and W. Nurul, *Mater. Sci. Forum*, 2019, **964**, 199–208, DOI: 10.4028/www.scientific.net/MSF.964.199.
72 S. Krachuamram, P. Kidkhunthod, Y. Poo-arporn and K. C. Chanapattharapol, *ChemEngineering*, 2024, **8**, 28, DOI: 10.3390/chemengineering8020028.
73 A. N. Chishti, F. Guo, A. Aftab, Z. Ma, Y. Liu, M. Chen, J. Gautam, C. Chen, L. Ni and G. Diao, *Appl. Surf. Sci.*, 2021, **546**, 149070, DOI: 10.1016/j.apsusc.2021.149070.
74 B. M. Trost, *Science*, 1991, **254**, 1471–1477, DOI: 10.1126/science.1962206.
75 R. A. Sheldon, *Green Chem.*, 2017, **19**, 18–43, DOI: 10.1039/C6GC02157C.